Biosensors and Bioelectronics 196 (2022) 113737

Contents lists available at ScienceDirect

Biosensors and Bioelectronics

journal homepage: www.elsevier.com/locate/bios

A plug, print & play inkjet printing and impedance-based biosensing technology operating through a smartphone for clinical diagnostics

Giulio Rosati [a], Massimo Urban [a,b], Lei Zhao [a], Qiuyue Yang [a], Cecilia de Carvalho Castro e Silva [a,c], Stefano Bonaldo [d], Claudio Parolo [a], Emily P. Nguyen [a], Gabriel Ortega [e], Paolo Fornasiero [b], Alessandro Paccagnella [d], Arben Merkoçi [a,f,*]

[a] Catalan Institute of Nanoscience and Nanotechnology (ICN2), Edifici ICN2, Campus UAB, 08193, Bellaterra, Barcelona, Spain
[b] University of Trieste, Department of Chemical and Pharmaceutical Sciences, Via Giorgieri 1, Italy
[c] MackGraphe-Mackenzie Institute for Research in Graphene and Nanotechnologies, Mackenzie Presbyterian University, Consolação Street 930, 01302-907, São Paulo, Brazil
[d] Department of Information Engineering, University of Padova, Via G. Gradenigo 6b, 35131, Padova, Italy
[e] Department of Chemistry and Biochemistry, And Center for Bioengineering. University of California Santa Barbara. Santa Barbara CA, 93117, USA
[f] Catalan Institution for Research and Advanced Studies (ICREA), Passeig de Lluís Companys, 23, 08010, Barcelona, Spain

ARTICLE INFO

Keywords:
Nanofunctional inks
Inkjet-printed sensors
Aptasensors
Flexible electronics
Impedimetric biosensors
Smartphone readout

ABSTRACT

Simplicity is one of the key feature for the spread of any successful technological product. Here, a method for rapid and low-cost fabrication of electrochemical biosensors is presented. This "plug, print & play" method involves inkjet-printing even in an office-like environment, without the need of highly specialized expertise or equipment, guaranteeing an ultra-fast idea to (scaled) prototype production time. The printed biosensors can be connected to a smartphone through its audio input for their impedance readout, demonstrating the validity of the system for point-of-care biosensing. Proper electrodes layout guarantees high sensitivity and is validated by finite element simulations. The introduction of a passivation method (wax printing) allowed to complete the devices fabrication process, increasing their sensitivity. Indeed, the wax allowed reducing the interference related to the parasitic currents flowing through the permeable coating of the employed substrates, which was used for the chemical sintering, thus avoiding the common thermal treatment after printing. As a case study, we used the devices to develop an electrochemical aptamer-based sensor for the rapid detection of neutrophil gelatinase-associated lipocalin (NGAL) in urine – a clinically important marker of acute kidney injury. The aptasensor platform is capable of detecting clinically relevant concentrations of NGAL with a simple and rapid smartphone readout. The developed technology may be extended in the future to continuous monitoring, taking advantage of its flexibility to integrate it in tubes, or to other diagnostic applications where cost/efficiency and rapidity of the research, development and implementation of point of care devices is a must.

1. Introduction

Biosensors first entered the market several decades ago and today - at the interface between research and the market - there is a plethora of new generation biosensors with the potential to profoundly influence medical decision-making. Applications of point-of-care (POC) diagnostics (C. Parolo et al., 2020), such as wearables for non-invasive health and lifestyle monitoring (Christodouleas et al., 2018), and the Internet of Things (IoT) network of environmental sensors, measuring the purity of our atmosphere, water and soil (Jaiswal and Anand, 2021), are on the rise. However, as technology becomes increasingly complex, simple and customizable fabrication of ultra-low-cost sensors together with user friendly testing in any environment is highly sought after. Currently, the production of biosensors is generally expensive, as specifically designed facilities (e.g., clean rooms) are required. Moreover, the need for trained personnel and specialized materials, as well as the time taken for production can further drive up costs. Thus, to enable widespread integration and accessibility to advanced POC technologies,

* Corresponding author. Nanobioelectronics & Biosensors Group, Institut Català de Nanociància i Nanotecnologia (ICN2), CSIC and The Barcelona Institute of Science and Technology (BIST), Campus UAB, 08193, Bellaterra, Barcelona, Spain.
E-mail address: arben.merkoci@icn2.cat (A. Merkoçi).

https://doi.org/10.1016/j.bios.2021.113737
Received 14 September 2021; Accepted 25 October 2021
Available online 29 October 2021

the fabrication process should aim to reduce costs to manufactures and, ultimately, everyday users.

Inkjet printing and smartphone sensing are promising candidates to fulfil these requirements, with the first allowing mass fabrication at low cost, and the second enabling easy POC and even at-home applications (Da Silva et al., 2014; Hernández-Neuta et al., 2019; Manoto et al., 2020; Medina-Sánchez et al., 2014; Quesada-González and Merkoçi, 2017). Inkjet printing represents as a highly cost-effective, user-friendly and versatile method for the fabrication of biosensors. In comparison to other printing fabrication methods, such as screen printing, the internal multichannel ink reservoirs can be adapted to print with many and various types of ink (i.e. conductive, dielectric etc.) and is well suited for various flexible substrates, such as paper and plastics (i.e. PET). Furthermore, inkjet printing also allows for mass production of biosensors with the capability to automate the printing process (Rosati et al., 2019a). Despite these excellent properties, inkjet devices fabrication is still bound to a laboratory-based paradigm, preventing its full potential as a ubiquitous production method to be exploited. This is mainly due to the treatments needed by the devices after printing. Thermal or optical procedures are in fact usually required to achieve the desired electrical and mechanical properties of the devices, such as thermal sintering on nanoparticles-based inks or photonic curing of insulating and polymeric inks (Cummins and Desmulliez, 2012; Wünscher et al., 2014).

Inkjet manufacturing is particularly convenient for the fabrication of affinity-based electrochemical label-free biosensors (Sui and Zorman, 2020; Tortorich et al., 2018). These are composed by electrodes modified with biological receptors that specifically bind the target molecule (affinity) if present in the liquid sample. The binding is detected with electrochemical techniques, such as impedance, that can be performed directly in the sample solution, without the addition of any further compound or label (label-free). Aptamers, which are short DNA sequences iteratively selected for their specific affinity to the target molecule of interest, are very proficient as bioreceptors due to their high stability, low-cost, and customizability, which makes them an excellent choice for this and other kinds of biosensors (Arroyo-Currás et al., 2017, 2020; Idili et al., 2019; Claudio Parolo et al., 2020). Electrochemical label-free and redox-free strategies, are typically considered prone to interference. Impedance aptamer-based affinity systems are no exception. Despite this, the level of interference mainly depends on two factors: the amount of interfering molecules present in the sample of interest (the so-called matrix effect), and the implementation of anti-fouling strategies and materials. Based on the expected level of interference in the sample of interest, different antifouling strategies may be considered. Between them, surface modification with Self-Assembling Monolayers (SAM) is probably the most diffused one. Several molecules can serve to this scope (Lin and Li, 2020). Despite that, also microfluidic and electrochemical protocols proved to be effective, e.g. continuous flow conditions or nanoshearing (Vaidyanathan et al., 2014).

In response to the need for a manufacturing technology that allows for convenient, cheap and easily transferable manufacturing of electrochemical biosensors, in this work, we propose a reliable Plug, Print & Play technology – plug: office-like equipment (no specific skills/laboratory needed), print: ease of design and of production by simply printing an image, & play: connection of the device to a smartphone and the simple drop-casting of the sample for immediate testing. We use this technology for the fabrication of aptamer-based biosensors for both office-like environments and POC testing. Hitherto, this goal has proved challenging from a technical/technological point of view due to the need for controlled operations/conditions and skilled personnel. In order to simplify these constraints, we introduced an innovative sinter-free method to produce electrochemical impedance-based devices. These, combined with a simple and cost-effective (~$5) circuit connected to the audio and microphone channels of a smartphone, and a commercial app, allow for fast impedance measurements at the point of care. To prove its validity for biosensing purposes, we functionalized the fabricated sensors with aptamers specific for NGAL (Azzalini et al., 2016; Wang et al., 2017), an early biomarker correlated to important syndromes such as acute kidney injury (AKI) and acute to chronic liver failure (ACLF, Kara et al., 2010; Mishra et al., 2004). Our inkjet sensors showed excellent performances in the clinical range (3–30 nM), with a sensitivity of 31.49 Ohm/nM, corresponding to a LOD of 3 nM in artificial urine. Furthermore, our biosensor proved to be resilient to the interference of Bovine Serum Albumin, which we used to emulate the presence of albumins which are one of the most typical class of protein found in human urine (Cheng et al., 2012). Therefore, effective impedance-based smartphone biosensors can not only be used at the PoC, but also produced by anyone with just office equipment (an inkjet printer, a wax printer, and a laminator).

In the following, we present our journey in the development and characterization of our Plug, Print & Play technology (Fig. 1). Starting from the materials selection (inkjet printer model and ink/substrate), we then characterized the printed lines morphology and conductivity, defining the parameters we needed for the electrodes design. We validated the design with FEM simulations to assess the uniformity of the electrical field along the electrodes and guarantee satisfactory performances in affinity sensing. Once theoretically validated, we produced the devices and we optimized their fabrication to avoid parasitic effects during the impedance measurements due to the semi-permeable substrate allowing room temperature sintering. The sensitivity of the impedance measurements to the coverage of the electrodes surface by biomolecules have been experimentally assessed and modelled by data fitting to an equivalent electrical circuit (EEC). Finally, we modified the devices with the NGAL specific aptamers and we performed the smartphone-based quantification.

The proposed detection mechanism, simply based on the non-faradic (label-free and redox-free) impedimetric detection of the NGAL binding to the aptamers immobilized on the electrode surface, is usually considered prone to unspecific binding and interference in real samples. Despite that, the combination of this detection method with well-characterized additional methods such as anti-fouling strategies, nanoshearing, and differential measurements, can guarantee very good performances for clinical testing, allowing also for the compensation of inter and intra-patient samples variations (McGrath et al., 1995; Sabaté del Río et al., 2019; Vaidyanathan et al., 2014). All the previous technologies can be easily exploited adding up additional electrodes in the design, i.e. asymmetric interdigitated electrodes for the nanoshearing and a second couple of the electrodes functionalized with similar but non-specific aptamers for differential measurements to remove the interferences due to the variability of the real samples.

2. Material and methods

Device fabrication and testing: The devices were fabricated following three procedures in order to compare the effect of two coating passivation strategies on electrochemical impedance measurements for affinity-based detection of biomolecules. Devices without any coating passivation were fabricated and tested as negative controls, as schematized in Fig. 2. All the device electrodes and contacts were inkjet-printed with Mitsubishi Paper Mills Silver Nano™ AgNP ink (NBSIJ-MU01) on Mitsubishi Paper Mills special substrate (NB-TP-3GU100) by an EPSON XP15000 printer. The surface was dried immediately after printing thanks to the substrates coating absorbing the ink solvent. We waited 72 h keeping the devices at RT before performing the following step to ensure proper drying of the solvent. The wax-passivated devices were fabricated by printing a layer of wax (black colour, Xerox Phaser 8850) in the area over and around the electrodes, with a 1 cm wide square pattern per each device. After the wax printing, we kept the device in the oven at 95° for 20 s to melt the wax and let it slightly penetrate the coating structure. We verified that this step could also be performed with a simple hairdryer without losing reproducibility since

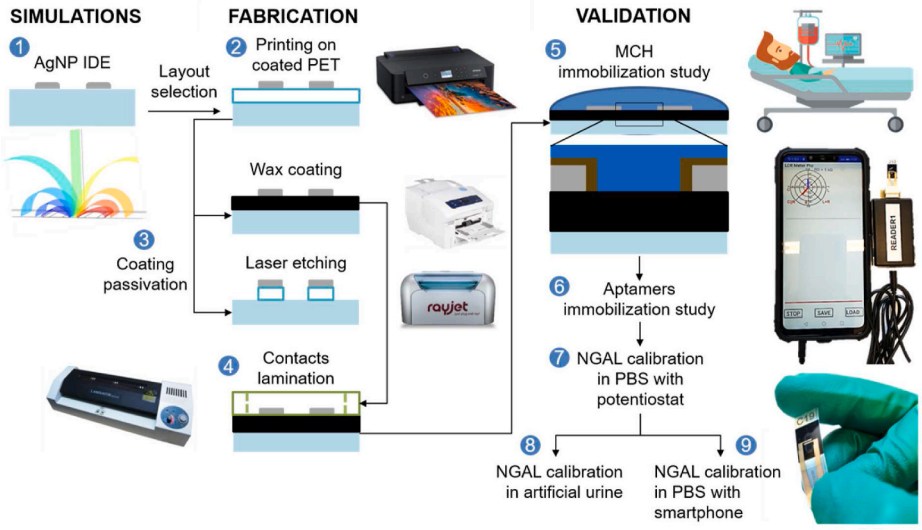

Fig. 1. The figure shows the steps in the process of the inkjet devices simulation, fabrication and optimization, and validation. The interdigitated electrodes (IDE) layout was selected thanks to the simulations (1) and inkjet-printed with silver nanoparticles (AgNP) ink on coated substrate for room temperature sintering (2). Two coating passivation strategies have been tested (3) and the devices were then laminated with patterned plastic sheets for contacts insulation (4). Bare, wax and laser etched devices were tested with mercaptohexanol (MCH) Self-Assembled Monolayer immobilization to select the most effective passivation method (5). Wax passivated devices were functionalized with NGAL Aptamers (6) and used to detect NGAL in Phosphate Buffered Saline (PBS) (7) and artificial urine (8). Smartphone measurements were performed on the same devices for the calibration of NGAL in PBS.

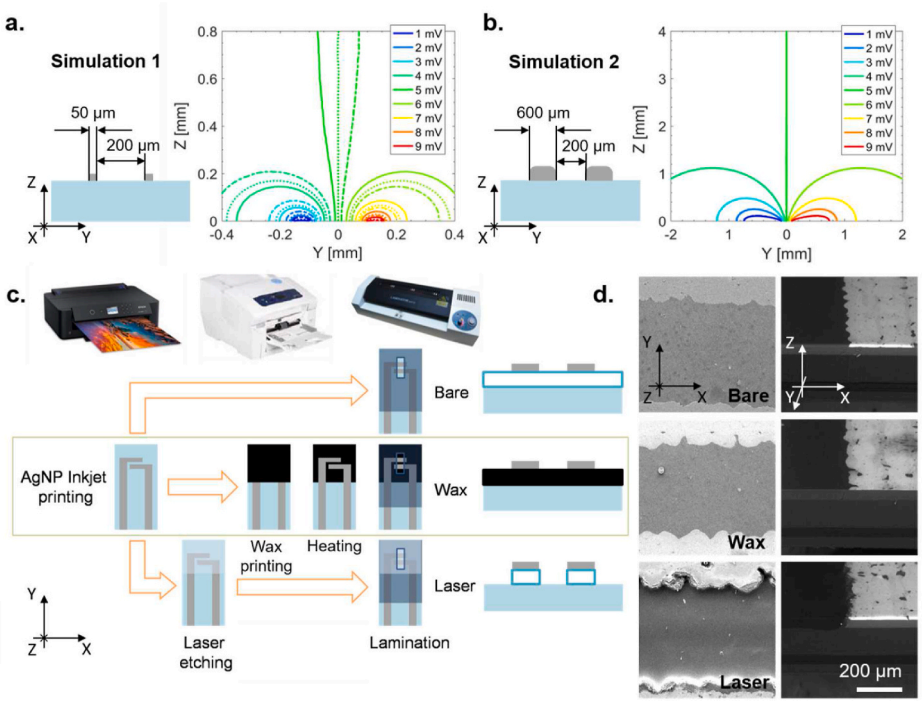

Fig. 2. The figure shows examples of the FEM simulation results for the layout described in the text and sketches the steps of the fabrication processes which has been tested, with the used equipment and SEM pictures of the resulting devices. a, cross-section sketch and contour plots of the electric field along the 50 µm wide electrodes at the base (continuous), middle (dashed), and end of the fingers (point-dashed). b, same representations of (a) for the 400 µm wide electrodes. c, Schematic of the fabrication steps of the bare, wax-passivated and laser etched devices. d, Corresponding SEM images of the gap between the printed electrodes and of the electrode/substrate cross-sections for the bare, wax and laser devices (from top to bottom, the images all have the same scale).

its goal was just to obtain a strong attachment between the wax and the coating. After this, we performed the deposition of a second wax layer to ensure a complete coverage of the area and we kept the devices in the oven for 5 min (this step can also be performed with an hairdryer).

The laser-etched devices were fabricated engraving the inkjet-printed devices with a Rayjet 50™ CO2 laser (power: 17%, speed: 100%, number of passages: 3) using the same PDF file employed for the wax printing. The laser vaporized the coating in the engraved area but not under the silver electrodes, which protected the coating reflecting the beam.

All the devices (inkjet-printed, wax-passivated, and laser-etched) were then laminated with a laser-patterned 100 µm thick lamination sheet (Fellowes A4 80 µm gloss) at the temperature recommended by the laminator manual for sheets of this thickness (temperature selector in orange position), exposing the device contacts and the electrodes in a 2 mm wide and 4 mm high window, through which the electrodes could come in contact with the solution. As performed in a previous study (Rosati et al., 2019b) the lamination sheet can also be patterned by a low-cost digital blade cutter (e.g. CraftROBO CC330), which can be safely used in any office-like environment (Fig. S5).

The fabricated devices were tested in 10 mM PBS (Merck-Sigma Aldrich) by drop-casting 50 µl of the solution on the active window and connecting them to a Metrohm AutoLab PGSTAT12 (FRA2) potentiostat by a custom adapter using a FPC Molex connector to ensure proper electrical contact. The Electrochemical Impedance Spectroscopy (EIS) measurements were performed in triplicate (if not otherwise specified) between 0.1 Hz and 100 kHz, 5 pt/dec, with 10 mVpp AC and 0 V DC. The open circuit characterizations were performed by repeating the EIS measurements with the described method three times: before the solution dropcasting (Open Circuit dry – OC dry), after the solution dropcasting (PBS), and immediately after the solution removal with nitrogen (Open Circuit wet – OC wet).

MCH functionalization, testing and EIS data fitting: All the fabricated device types were modified by incubating them in 50 μl mercaptohexanol (Merck-Sigma Aldrich) dilutions in 10 mM PBS for 1 h at RT. The dilutions ranged from 10 nM to 10 mM, one per decade. After the incubation period, the devices were washed with milliQ and dried with nitrogen. Then, the devices were tested by EIS with the same settings described in the previous paragraph. On the basis of the impedance data we got from the PBS characterization and considering both the nature of conduction through the solution and through the wet coating, we defined an electrical equivalent model (Fig. 4b). The EIS data collected from the MCH-modified devices were fitted with the defined model with ZView2™ (Scribner's and associates).

Aptamer immobilization: The NGAL aptamers were designed and selected by the Plaxco group and were composed of a thiol-modified end. They were reduced in Tris(2-carboxyethyl)phosphine hydrochloride (TCEP) 10 mM for 1 h in the dark and then diluted in 10 mM PBS with 1 mM $MgCl_2$ to 1000 nM. From this concentration, we prepared two other dilutions, respectively of 100 and 10 nM. The wax-passivated devices, selected for the following tests thanks to the MCH tests and data fitting, were incubated for 2 h drop-casting 50 μl of the three aptamer dilutions. After the incubation, the devices were washed with milliQ and dried with nitrogen. Before testing the devices, we waited for 3 h, keeping them at RT to ensure a complete drying of any liquid residue eventually infiltrated under the wax layer. The functionalized devices were tested by EIS in 10 mM PBS (in triplicate) with bare wax-passivated electrodes tested as negative control (Fig. 5a).

NGAL detection: The aptamer-functionalized devices were separately tested by EIS in 5 NGAL dilutions ranging from 0.3 to 3000 nM and in PBS. Each dilution was tested on three devices for each aptamer concentration. The 10 nM and 1000 nM aptamer concentrations did not show a clear response to the NGAL dilutions, while the 100 nM aptamer showed a good response at frequencies in the range between 1 and 100 Hz. Therefore, 100 nM aptamer concentration and 100 Hz were selected for the device calibration.

The calibration was performed by connecting 6 devices to the AutoLab multiplexer module (MUX) and setting up a customized NOVA function for the continuous measurement of impedance at 100 Hz. We dropcasted 50 μl of 10 mM PBS on all the devices and we started the impedance measurements. After 10 min we replaced 25 μl of the drop on the devices with the first NGAL dilution on three of the six devices, and with PBS on the other three. We repeated the procedure for each NGAL dilution, with a 10 min interval between each substitution.

The staircase calibration data was analyzed by subtracting the data of the PBS sensors from the NGAL ones to compensate the eventual drift related to the long measurements (almost 2 h). The added NGAL concentrations are reported in Fig. 6a. However, the effective NGAL concentration on the sensor was generally slightly higher than half the added concentration due to the half drop replacement protocol. The kinetics related to four NGAL concentrations between 0.15 and 25.10 nM were fitted to a mono-exponential equation.

The smartphone NGAL measurements were performed with the same staircase calibration protocol but taking full 50 Hz–20 kHz impedance spectra from three Android 8.1.0 smartphones (Huawei Mate 20 lite) connected to three identical reader circuits. Every EIS measurement was taken after 10 min of incubation with the respective NGAL dilution. The calibration curve was obtained plotting the impedance module at 150 Hz (Fig. 6c). The data was fitted using the Hill equation. Finally, the same measurements were repeated in artificial urine (Surine Negative Urine Control, Sigma).

3. Results and discussion

3.1. Materials selection and consumer printer setup

The printer selected for the new developed platform was the Epson XP 15000. The main advantages of this printer model are the minimum drop volume of about 5 pl, the availability of empty cartridges on the market, the relatively low cost of the printhead, and the recent date of entrance in the market to ensure the longest availability of the printer on the market. Table S1 lists the settings used for the printing with Epson XP15000.

Regarding the inks and the substrates used for the printing, the choice of conductive inks is fundamental to define the electronic and electrochemical properties of the printed electrodes. Following the principle of an easy and user-friendly fabrication platform, we checked the commercially available inks based on different metal nanoparticles, i.e. mainly gold and silver. However, only the widespread silver-nanoparticles-based inks (AgNPs) were found to meet the requirements of a sustainable price-over-quantity ratio, sufficient ease of management, and long-term stability at room temperature (RT). The main producers of inkjet AgNP-based inks are Mitsubishi Paper Mills and Novacentrix, which also produce the semi-absorbing plastic substrates, typically used with these inks for the high-quality printing of electronics. Semi-absorbing plastic substrates guarantee the chemical sintering of the AgNPs at RT, where a reagent in the absorbing coating of the substrates remove the outer protective shell of the nanoparticles and drastically improve their conductivity. Inks were tested in combination with several substrates and their printing performance was compared in terms of minimum conductive width of the electrode lines (or fingers) and their resistance with respect to the printing direction. The study, based on a previous work (Rosati et al., 2019b), allowed us to select the Mitsubishi ink and substrate for the following steps.

3.2. Printed lines morphology and conductivity

In order to evaluate the printing results of the Epson printer, we performed an analytical comparison with a standard Dimatix 2800 printer. The lines printed with the Mitsubishi AgNP ink on the respective substrate were characterized by optical microscopy and interferometric measurements (Fig. S1). Despite the Dimatix's lines appear more uniform, the Epson reached similar resolution and conductivities (Figs. S1 and S2), and even a much faster resistance stabilization time. The interferometric analysis clearly evidenced the single jetted drops in 3D, with an average drop diameter of about 20–30 μm and a thickness of between 125 and 200 nm (Fig. S1d). Furthermore, the thickness of a printed line significantly varied through its width. In fact, the central regions of lines had a thickness of ~800 nm, while their lateral borders had a thickness of ~150 nm. This difference is related to the different number of overlapped layers of jetted drops, as the printer overlaps 4 different layers at a distance of more than 150 μm from the line border.

This 3D profile of the lines implies that lines with widths lower than 300 μm have a significantly different thickness and thus conductance with respect to larger ones. In turn, this explains why the resistance of 2 cm lines of different widths did not follow Ohm's first law for lines under the 300 μm (Fig. S2). In these cases, the terrace-like 3D structure of the jetted drops along the line section strongly influences the lines' resistances. Moreover, optical characterizations of the lines (Fig. S1) evidenced several defects on the overlapping of drops along the line, creating bottlenecks between two consecutive drops, which inhibit the electric conduction. It is important to underline that the precision of the overlapping of the drops strongly depends on the printing direction. As studied in one of our previous works (Rosati et al., 2019a), the highest quality is obtained when the lines are printed along the same direction of the printhead movement, called "inline"-print, while the worst quality is perpendicular to it, called "outline"-print (Fig. S1a).

All the electrodes fabricated in this study were printed "inline", in order to obtain the highest quality in terms of precision and reproducibility. The measured resistivity for lines of width greater than 300 μm resulted in 0.685 μΩm, corresponding to 2.32% of the bulk silver conductivity. Only the contacts were printed "outline", as their extended area with large width neutralizes the weight of defects on the line resistance.

Another important element to consider is the difference between the layout width and the real width of the lines (Fig. S2a). The real printed lines were generally 1.34 times wider than the nominal layout value with an offset of 85 μm, as obtained from the linear regression. However, this law was not respected only for nominal dimensions lower than 100 μm and a minimum printable width of 50 μm. Based on these analysis, we defined equivalent profiles for 400 μm nominal width lines and for the thinnest printable lines.

3.3. Electrodes design and simulations

For our device, we chose a simple 2 interdigitated electrodes design. As a first step, our devices are characterized by two parallel electrodes with a nominal width of 30 μm (real width = 50 μm), a gap of 200 μm and a total length of 2 mm, since this was the minimum printable width for a conductive line. However, we found that, even though thinner electrodes are typically associated with higher sensitivity, this scaled design may result in a not-uniform electric field along the electrodes. This effect is due to the balance between the lines conductance and the conduction through the liquid sample over the electrodes, as described in a previous work [23]. The electric field uniformity is important in the development of electrodes in order to guarantee an equal sensitiveness of all regions of the electrode surface. Therefore, we designed and printed two other electrodes with nominal widths up to 400 μm (real width = 600 μm) and the same 200 um gap between the electrodes (Fig. S3a). The real gap distance has been kept constant in the two layouts introducing an offset proportional to the theoretical width to compensate the spreading of the printed lines on the substrate.

To further verify the optimization of the electrode design, simulations using COMSOL Multiphysics™ were conducted to simulate their electrical behaviour and, in particular, observe the uniformity of the electric field along the electrodes. Using the morphological and electrical characterizations described in paragraph 2.2, we modelled the electrode-solution interface. The mesh of the electrodes had the previously defined profile and conductivity on a dielectric substrate. The electrodes were surrounded by a 3D rectangle, which simulates the solution drop over the electrodes. The base dimension of the rectangle equalled that of the device active window with a width of 2 mm and a height of 4 mm (Fig. S3b). We set the conductivity of the 3D rectangle to 16 mS/cm, equal to the conductivity of 10 mM PBS, used for the EIS measurements.

Simulation of the electric potential along the meshed electrodes allowed us to check for its uniformity when an electrical stimulation of 10 mV DC was applied between the two electrodes ends. This study was fundamental to assess if variations of impedance due to passivation of the electrodes by the binding of the analyte to the functionalized surface was equally effective along the electrode length. A uniform field would mean a smaller impedance signal variation due to the same analyte concentration in solution.

The potential isosurfaces, shown in Fig. S3d, reveals a non-uniform electrical field along the electrodes for the 50 μm layout. This is even more evident in Figs. 2a and S3e, which underlines the non-overlapped contour plots in different planes along the electrodes. The width and gap between the electrodes is paramount to define the field uniformity. For example, a nominal width of 400 μm with a gap of 200 μm with mesh shown in Fig. S3f resulted in a uniform electrical field as can be seen from both the isosurfaces and contour plots in Fig S3g, 3b and S3h. The trade-off between the field uniformity and the reduction of the surface area of the electrodes is fundamental to ensure the highest signal variation related to the analyte binding on the electrodes (Rosati et al., 2014).

3.4. Fabrication of the biosensors and initial electrochemical validation

After choosing the validated 400 μm device layout, we studied and optimized the devices fabrication process in order to obtain the best impedance-based electrochemical detection performance. The focus of this process is the removal or passivation of the absorbing coating on the substrate. Indeed, the coating guarantees a rapid and precise printing with an RT chemical sintering and also absorbs any liquid solution in contact with it. The solution penetrates and slowly diffuses around the electrodes causing instabilities and undesired short-circuiting effects. Even if the "short-circuit" resistance has values in the order of 100 kOhm, this prevents the devices from optimally performing affinity-based detection of the analyte.

As illustrated in Fig. 2, we compared two strategies for the coating passivation/removal with the bare devices (with the coating intact and unmodified). In the first strategy, two layers of wax ink were deposited over the electrodes around the solution interface area and heated up to penetrate in the coating. While, in the second strategy, the corresponding area was etched by a desktop CO_2 laser.

The wax devices appears clearly black and the fact that their SEM images show a similar surface to the bare devices indicates that the wax effectively penetrated in the coating, even if in the cross-section image no difference between the coating and wax can be distinguished. This is due to the similar density and elemental composition of the two materials. SEM images acquired at higher magnification and lower acceleration voltage allowed us to slightly distinguish the two (Fig. S4), further proving the permeation of the coating by wax.

Interestingly, the laser was reflected by the AgNP electrodes and as a result, the substrate coating beneath them remained intact (bottom SEM pictures of Fig. 2).

All the devices (bare, wax and laser) were then encapsulated in a laser-patterned lamination sheet in order to define the sensor active window, where the two parallel electrodes were exposed to the testing solution. The lamination sheet can be also patterned by office-like cheaper equipment such as digital cutter. There is no need for a laser cutter for this as demonstrated in a previous work (Rosati et al., 2019a).

We carried out 3 studies to verify the most effective coating passivation strategy and compare the device performance: 1) we simply measured the impedance spectra in 10 mM PBS; 2) we compared the impedance of the dry electrodes with the that of the electrodes dried right after a measurement in PBS; and 3) we studied the sensor impedimetric response to the functionalization with 6-Mercapto-1-hexanol (MCH) dilutions ranging from 10 nM to 10 mM.

EIS measurements are used to characterize the printed electrodes. Such measurements are minimally perturbing the electrochemical cell, thus it is possible to avoid the use of a reference electrode. In this way, the device can be composed of just 2 identical electrodes. Moreover, we did not use any redox mediator on our sensors, allowing direct measurement of the sample solutions, without any pre-treatment. In this configuration, the binding of biomolecules on the electrodes surface is usually detected as an increase of the impedance module at the frequencies resulting in the phase peak, i.e. where the impedance spectra is dominated by the double-layer capacitance of the electrochemical cell. However, electrodes printed on porous substrates could be affected by the parasitic conductance of the solution infiltrating under the electrodes and limiting the maximum increase of impedance achievable with their top surface coverage with the biomolecules of interest. From this, the rationale of the substrate coating passivation strategies is the reduction of these parasitic components.

The wax-passivated devices EIS response (Fig. 3a) clearly shows a higher impedance with respect to the bare electrodes at low frequencies. The laser-treated devices surprisingly show lower impedance values in the same region. In the high-frequency range, where the impedance response is mainly related to the resistance of the solution, the curves are relatively similar. This indicates that the modification of the devices did not significantly change the electrode surface and interaction with the solution. However, the spectra of all the devices show a phase peak around 20 Hz, which is not coherent with the R–C behaviour expected in PBS not containing any redox probe.

The EIS tests on the dry electrodes before and after the PBS

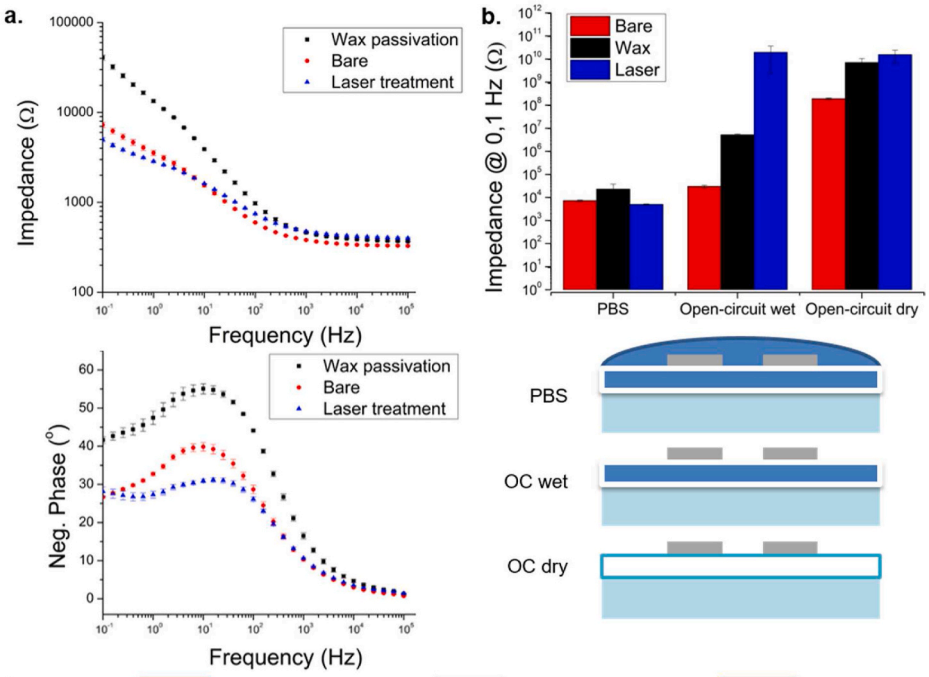

Fig. 3. The figure represents the EIS responses of the fabricated devices (bare, wax-passivated and laser-engraved) in order to define the most effective coating passivation method. a, Bode diagrams of the devices' impedance spectra measured in PBS. b, Comparison of the 100 mHz impedance modules of the devices in PBS, immediately before the PBS injection, and immediately after it. c, Schematics illustrating the theorized conduction between the bare, wax-passivated and laser-treated electrodes.

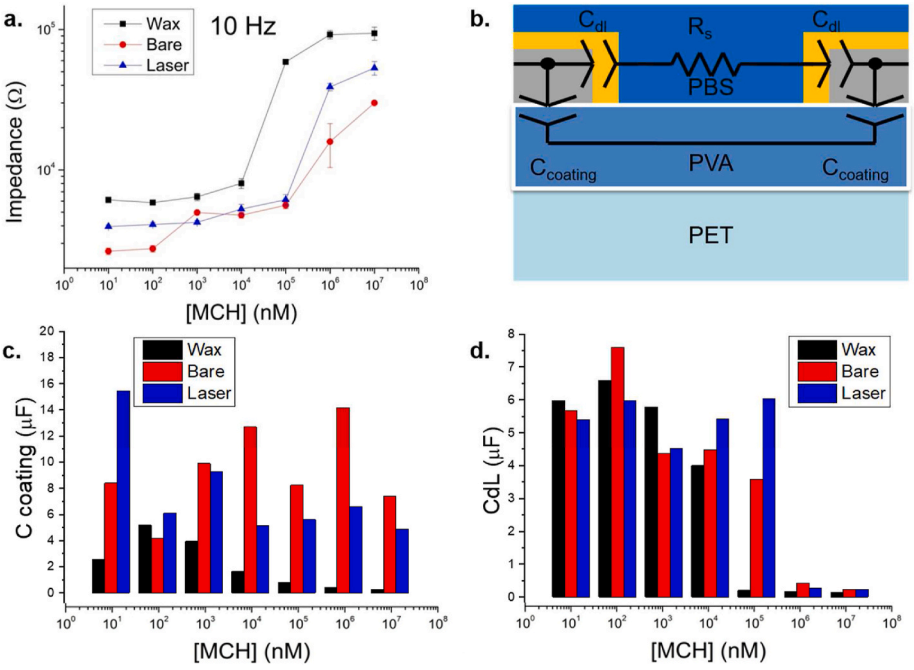

Fig. 4. Impedance spectra and modelling of the bare, wax-passivated and laser-etched devices modified with a MCH self-assembled monolayer. a, Impedance modules at 10 Hz recorded for bare, wax-passivated and laser-etched devices. b, Electrical equivalent circuit and schematic of the devices model of conduction. c,d EEC parameters values with respect to the MCH concentration for the bare, wax-passivated and laser-etched devices. The values have been obtained by fitting the average impedance spectra in the three cases, so no standard deviations are reported. The percentage errors obtained for the two elements were smaller than 5% in all the cases.

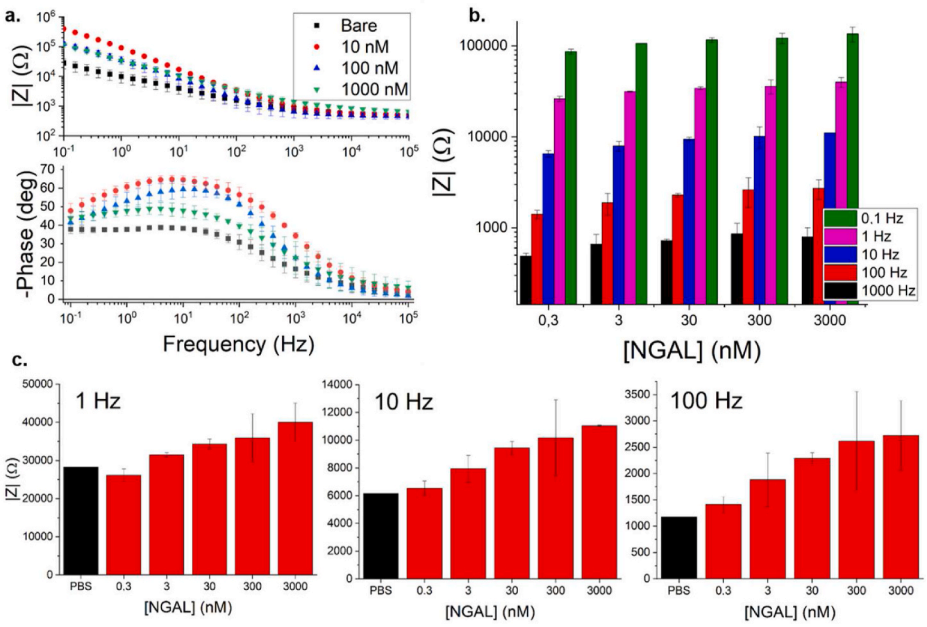

Fig. 5. NGAL aptamer concentration optimization and detection testing. a, Impedance module and phase spectra obtained after the functionalization with 10, 100 and 1000 nM NGAL aptamer (N = 3). The 10 nM case probably resulted with the highest impedance module values because the aptamers may be lying horizontally with a so low packing density and no spacer. b, Average impedance module values with respect to NGAL concentration at 0.1, 1, 10, 100, and 1000 Hz for the aptasensors functionalized with 100 nM NGAL aptamer. c, Single frequency plots of the data in b. for the frequencies 1, 10 and 100 Hz (N = 3) compared to measurements in PBS for a better visualization of the impedance values dependence on the NGAL concentration. The error bars represent the standard deviations in all the plots and in some case are relatively big because of a possible lack of reproducibility between the three different devices used for each concentration.

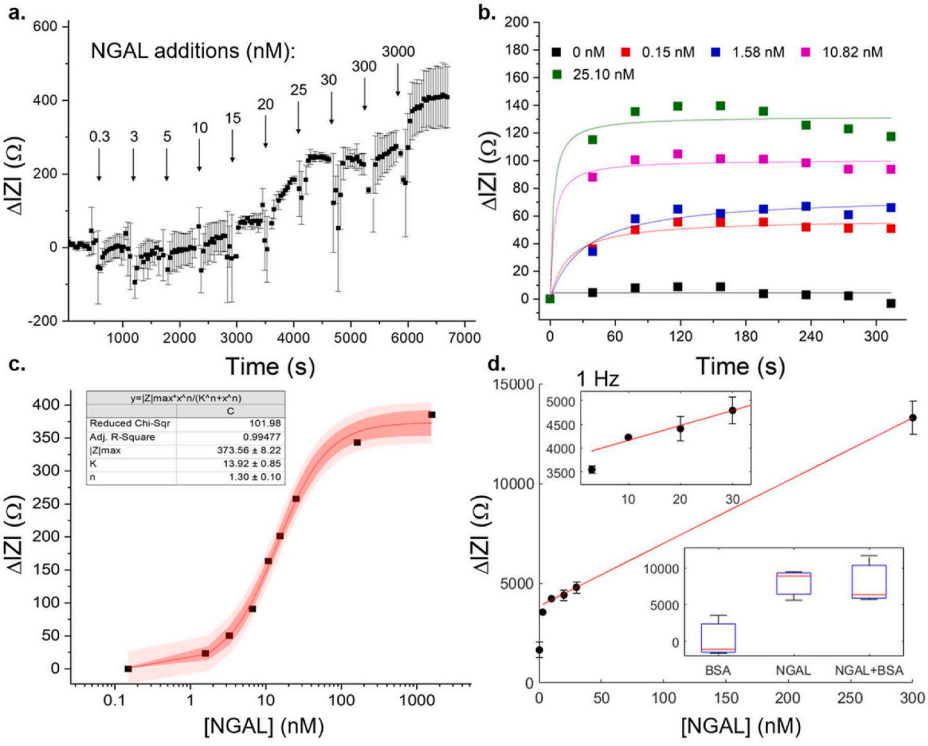

Fig. 6. NGAL calibration on the impedance aptasensors. a, Staircase NGAL calibration in PBS at 100 Hz by potentiostat with the injected NGAL concentrations in the PBS drop over the aptasensor b, Kinetics associated to the effective NGAL concentrations in the drop in the first seconds after the injection and respective fitting with single exponential equation. c, Smartphone-measured NGAL calibration curve at 100 Hz with Langmuir fitting ($|Z|_{max}$ = 373.56, K = 13.92, n = 1.30, Adj. R^2 = 0.99477) and 95% confidence and prediction bounds. d, NGAL detection in artificial urine, impedance module variation at 1 Hz with respect to pure artificial urine with linear fitting of the values in the range 3–300 nM ($\Delta|Z|$ = 31.49[NGAL]+ 3845, R^2 = 0.9998). In this case, due to the change of the buffer properties, the response at 1 Hz resulted more significative with respect to the one at 100 Hz. The top inset shows a magnification of the 0–30 nM range and the bottom inset shows the result of the interference study performed with BSA.

measurements (Fig. 3b) gave further tips to understand the real nature of the events taking place at the electrode interfaces and inside the coating. As expected, the bare devices showed a difference of 4 orders of magnitude between the 0.1 Hz impedance modules of the dry electrodes before and after PBS testing. The wax-passivated devices significatively increased the impedance absolute values and reduced the difference between the two conditions to 3 orders of magnitude. While, the laser-treated devices showed the highest impedance module values and completely closed the gap between the dry measurements before and after PBS testing, saturating the potentiostat at this frequency (10 GOhm).

These results evidence what is happening in the three types of tested devices. Fig. 3c illustrates the hypothesized behaviour of the electric field between the electrodes of the three device types. The bare devices coating between the two electrodes immersed in solution is immediately penetrated by the solution, which diffuses under the bottom face of electrodes. The conduction through the coating is thus possible and, for low frequencies values, the EIS curve follows the trend of a constant phase element with a behaviour closer to that of a resistance with a negative phase lower than 30°. This reduces the impedance values in that region, dominating the double layer capacitance related one and forming a peak in the phase, like in a redox-based system. This

behaviour is confirmed by the impedance module values at 0.1 Hz on the dry electrodes after the PBS testing, which are just 1 order of magnitude greater than the ones recorded in PBS. For the laser-treated devices, the impedance of the dried electrodes after PBS testing is so high because the coating has been completely etched between the electrodes, thus nothing connects them when dried. However, the coating is still present under the electrodes and this does not solve the problem during the PBS measurements, which in fact appears similar or even worse than the bare device ones. In wax-passivated devices, the conduction through the coating is drastically reduced making it more hydrophobic even if not completely impermeable. The measurements on the dry electrodes clearly show a net improvement in the gap between the impedance modules at 0.1 Hz of the PBS test and of the dried electrodes, reaching almost 4 orders of magnitude. Even the impedance of the dry electrodes improved, reaching the values obtained with the laser treatment. This is clearly reflected in the PBS tests, with the phase reaching −55° even if still affected by a reduced coating conduction.

3.5. Impedance sensitivity to surface coverage and electrical modelling

The devices functionalization with mercaptohexanol (MCH) lipidic self-assembled monolayer allowed defining their sensitivity to surface coverage and a comparison of how it is influenced by the coating passivation method. The average impedance response of the functionalized devices showed its highest variations at 10 Hz (Fig. 4a). As expected, the impedance module increases with the MCH concentration, until reaching a plateau in correspondence with the highest concentrations. Comparing device impedance, the bare devices showed the lowest values, with a slow increase starting at 1 μM MCH and never really reaching a saturation value. The laser treated devices showed a similar behaviour but the impedance started from and reached higher values, with a sigmoid shaped curve. Conversely, the wax passivated devices showed the greatest impedance variation. Furthermore, this variation was achieved at a MCH concentration between 10^4 and 10^5 nM, at least one order of magnitude smaller with respect to the other two device types (between 10^5 and 10^6 nM). This indicates their highest sensitivity to surface coverage, thus offering the best detection performance for surface binding events, i.e. for affinity-based biosensing. Based on the collected data, an electric equivalent model was developed for bare, laser-treated and wax-passivated devices. The main part of the model (Fig. 4b) consisted of a simple series of the resistance of the solution (R_s) and the electrode double layer constant phase element (C_{dl}). No charge transfer resistance was added since the measurements were performed without any additional redox probe to allow direct sample testing, without any sample pre-treatment or solution addition. We added to this simple model a constant phase parasitic element ($C_{coating}$), which accounted for the conduction through the wet coating with phase values in the range 30-40°. The experimental MCH data were fitted to the model and the variation of its key parameters, as the double-layer capacitance and the coating parasitic capacitance are shown in Fig. 4c and d.

As the defined model in Fig. 3b indicates, the higher the coating impedance the more effective the coating passivation. With the absolute value of impedance inversely proportional to the capacitance, we would expect a better passivated device to have lower $C_{coating}$ values. In these terms, the fitting results in Fig. 3c prove again that wax offered the best passivation performance, while the C_{dl} clearly indicates how the wax-passivated devices increased their sensitivity to the surface modification by MCH (significant variation at 10 times lower MCH concentrations) with respect to the other two types.

3.6. Modification of biosensors with NGAL aptamers

As the wax-passivated devices showed the most promising results in the previous tests, we decided to functionalize them with aptamers specific for NGAL for real-time detection in urine. The device functionalization was performed simply by drop-casting the activated thiolated aptamers on the electrodes for 2 h. Three different aptamer concentrations were tested, ranging from 10 nM to 1 μM.

Fig. 5a shows a large variation in EIS responses between the bare electrodes and the 10 nM functionalized ones. While the variations between different concentrations of the aptamers (100 nM vs. 1 μM) are significant, they are smaller. As shown in Fig. 5b, we interpreted this result as the effect of the aptamers lying in a horizontal configuration, due to the lack of the repulsion between the nucleotides negative charges in such a dispersed solution. This configuration produced a greater coverage of the surface with a consequent decrease of the double layer capacitance and an increase of the related impedance module. Interestingly, in the case of 100 nM and 1 μM aptamers dilutions, the greatest variation between the respective spectra was observed around 100 Hz, instead at lower frequencies as observed for the other dilutions.

For all the aptamer-modified devices, we performed EIS measurements in NGAL dilutions in PBS. The tested NGAL concentrations range was between 0.3 nM and 3000 nM, covering the range of clinical interest (3–30 nM). The highest impedance variations were obtained with 100 nM aptamers (Fig. 5c), showing a maximum variation of more than 1.5 kOhm at 100 Hz and a range of detection between 0.3 and 30 nM. For higher concentrations, i.e., 300 and 3000 nM, the impedance variations saturated probably because of the full occupation of the available aptamers on the electrodes surface. This may have also caused in some case a partial disruption of the aptamers self-assembled monolayer due to electrostatic forces, increasing the variability of the results as can be seen from the higher errorbars.

3.7. Smartphone-based NGAL quantification

To prove the feasibility of continuous monitoring and real-time detection (Curtis et al., 2019), we performed the calibration on single electrodes injecting increasing NGAL concentrations over time and monitoring the impedance variation at 100 Hz. As previously proved by Parolo et al. (Claudio Parolo et al., 2020), these aptamers allow the monitoring of NGAL for hours if placed in a catheter. This is possible thanks to the aptamer affinity to the protein, which is strong enough to capture it but also weak enough to release it in presence of a moderate flow of the surrounding solution. Fig. 6a shows the average variations with the respective standard deviations over time, corresponding to the NGAL injections performed every 10 min. The maximum variation reached was with the 25 nM injection with a corresponding value of almost 300 Ohms. The calibration on single electrodes also allowed lowering the standard deviations, minimizing the effect of the devices reproducibility.

In the case of electrochemical biosensors, to guarantee POC use of the developed system, it is essential to push both towards the scalability of the proposed biosensor fabrication method and to the availability of portable and widespread instrumentation to perform the measurements and analysis. In our work, the first goal was accomplished with the simple “plug & print” approach for device production, which guarantees reliability and scalable low-cost production in office-like environments as well as a high level of customization (the total fixed and variables fabrication costs are presented in detail in Table S2, in the supporting information). To pursue the second goal, the smartphone with its widespread use and computational power is the best strategy. To this end, we used the audio and microphone channels of an Android smartphone and a commercially available app (Google Play link) together with a simple custom-made $5 electronic circuit to connect our devices to the smartphone and perform EIS measurements in the 50 Hz - 20 kHz frequency range.

We tested the devices with the same testing protocol previously used with the potentiostat (increasing NGAL injection concentrations every 10 min), but measuring the full spectra through the smartphone after 10 min of incubation. The impedance variations at 150 Hz (which resulted slightly less noisy rather than the 100 Hz values) are reported in Fig. 6c

and are coherent with the ones observed in Fig. 6a with the potentiostat. We also tested both setups for variations obtained by repeated injection of the buffer only on the functionalized devices, obtaining negligible variations over the whole duration of the test.

Finally, the NGAL detection sensor was tested with NGAL dilutions in artificial urine to emulate the environment of a real application. The results, represented in Fig. 6d, show a linear variation of the impedance in the 1–300 nM range. Furthermore, we tested our sensors with 30 nM BSA, 30 nM NGAL and 30 nM BSA+30 nM NGAL, obtaining the results resumed in the boxplot in inset of Fig. 6d. These results prove the biosensor reliability for the NGAL POC monitoring and its resilience to unspecific binding.

On the basis of the data obtained by the staircase calibration, after the analysis of the impedance variations referred to the blank measurements, we determined the performance of our biosensor by means of its sensitivity, linear range, and limit of detection. For the latter we needed to introduce an alternative definition. In general, the LOD is calculated as the analyte concentration that causes a signal variation greater to 3 times the standard deviation of the blank measurements. However, in our case the calibration curves are built as the variations of the impedance signal at a certain frequency with respect to the blank measurement. Therefore, the blank measurements result all at zero and a standard deviation value cannot be obtained. We decided to calculate the LOD as the first tested concentration causing an impedance variation greater than 3 times its standard deviation. This method should overestimate the actual LOD of the sensor but we think it is the more suitable for our type of calibration curves.

Also our sensitivity definition may appear unusual, particularly for its measurement unit. Despite that, in this case, we used the common definition, i.e., the slope of the linear part of the calibration curve, which in our case is measured in Ohms over NGAL concentration (Ohm/nanomolar).

Considered this, our biosensor showed a sensitivity of 31.49 Ohms/nM, a linear range from 3 to 300 nM and a LOD of 3 nM in artificial urine, considering the impedance variations at 1 Hz. In PBS and at 100 Hz, the biosensor showed a sensitivity of 7.92 Ohms/nM, a linear range from 3 to 30 nM and a LOD of 10 nM. Despite it may looks counterintuitive to obtain a better performance in artificial urine rather than in PBS, we recall that it strongly depends on the chosen frequency for the impedance variations analysis. The frequency optimization is thus a very important step, which needs to be performed in the final matrix to obtain the best performance results.

4. Conclusions

In conclusion, in this work, we designed a simple IDE layout and we simulated it by FEM, selecting optimal geometrical parameters on the base of the electronic characteristics of the AgNP lines. Then, we printed the IDE with a consumer printer and commercially available ink and substrate without any sintering step. These devices were then characterized with EIS measurements for use as affinity label-free and redox-free biosensors. We introduce and studied an effective method to reduce the parasitic conduction through the semi-permeable substrate coating allowing the room temperature sintering by using a consumer wax printer and we isolated the contacts of the devices by plastic lamination. Therefore, we introduced a complete biosensors fabrication platform using only office low-cost equipment. We used MCH SAM as a model to validate the sensitivity of the EIS devices to surface coverage by biomolecules. Finally, we functionalized the validated devices with NGAL aptamers as a proof-of-concept of their validity for biosensing purposes and we detected NGAL in PBS and artificial urine using a low-cost smartphone-based system in the clinical range for AKI continuous monitoring at the point of care.

Declaration of competing interest

The authors declare that they have no known competing financial interests or personal relationships that could have appeared to influence the work reported in this paper.

Acknowledgements

The development of the device fabrication platforms has been partially funded through the MICROB-PREDICT project (https://microb-predict.eu/).

The MICROB-PREDICT project has received funding from the European Union's Horizon 2020 research and innovation programme under grant agreement No 825694. This reflects only the author's view, and the European Commission is not responsible for any use that may be made of the information it contains.

We thank Dr Alex Chamorro and Prof. Kevin Plaxco for the NGAL aptamers sequence used for the case study of our biosensors. E. P. N. acknowledges funding through the EU's Horizon 2020 research and innovation programme under the Marie Skłodowska-Curie grant agreement No. 754510. C.C.C.S. acknowledges funding through CAPES – PRINT (Programa Institucional de Internacionalização; grant #88887.310281/2018-00 and 88887.467442/2019-00) and Mackpesquisa-UPM.

This project has received funding from the European Union's Horizon 2020 research and innovation programme under grant agreement No 101008701 (Project acronym: EMERGE)

Appendix A. Supplementary data

Supplementary data to this article can be found online at https://doi.org/10.1016/j.bios.2021.113737.

References

Arroyo-Currás, N., Dauphin-Ducharme, P., Scida, K., Chávez, J.L., 2020. Anal. Methods 12, 1288–1310. https://doi.org/10.1039/d0ay00026d.

Arroyo-Currás, N., Somerson, J., Vieira, P.A., Ploense, K.L., Kippin, T.E., Plaxco, K.W., 2017. Proc. Natl. Acad. Sci. U. S. A. 114, 645–650. https://doi.org/10.1073/pnas.1613458114.

Azzalini, L., Spagnoli, V., Ly, H.Q., 2016. Can. J. Cardiol. 32, 247–255. https://doi.org/10.1016/J.CJCA.2015.05.013.

Cheng, L., Lopez-Beltran, A., Bostwick, D.G., 2012. https://doi.org/10.1002/9781118275436.ch32.

Christodouleas, D.C., Kaur, B., Chorti, P., 2018. ACS Cent. Sci. 4, 1600–1616. https://doi.org/10.1021/acscentsci.8b00625.

Cummins, G., Desmulliez, M.P.Y., 2012. Circuit World 38, pp. 193–213. https://doi.org/10.1108/03056121211280413.

Curtis, S.D., Ploense, K.L., Kurnik, M., Ortega, G., Parolo, C., Kippin, T.E., Plaxco, K.W., Arroyo-Currás, N., 2019. Anal. Chem. 91, 12321–12328. https://doi.org/10.1021/acs.analchem.9b02553.

Da Silva, E.T.S.G., Miserere, S., Kubota, L.T., Merkoçi, A., 2014. Anal. Chem. 86, 10531–10534. https://doi.org/10.1021/ac503029q.

Hernández-Neuta, I., Neumann, F., Brightmeyer, J., Ba Tis, T., Madaboosi, N., Wei, Q., Ozcan, A., Nilsson, M., 2019. J. Intern. Med. 285, 19–39. https://doi.org/10.1111/joim.12820.

Idili, A., Parolo, C., Ortega, G., Plaxco, K.W., 2019. ACS Sens. 4, 3227–3233. https://doi.org/10.1021/acssensors.9b01703.

Jaiswal, K., Anand, V., 2021. In: Rizvanov, A.A., Singh, B.K., Ganasala, P. (Eds.). Springer Singapore, Singapore, pp. 459–471.

Kara, P., de la Escosura-Muñiz, A., Maltez-da Costa, M., Guix, M., Ozsoz, M., Merkoçi, A., 2010. Biosens. Bioelectron. 26, 1715–1718. https://doi.org/10.1016/j.bios.2010.07.090.

Lin, P.H., Li, B.R., 2020. Analyst 145, 1110–1120. https://doi.org/10.1039/c9an02017a.

Manoto, S.L., Mabena, C., Malabi, R., Ombinda-Lemboumba, S., El-Hussein, A., Kasem, M., Lugongolo, M., Mthunzi-Kufa, P., 2020. Proc.SPIE. https://doi.org/10.1117/12.2546444.

McGrath, M.J., Iwuoha, E.I., Diamond, D., Smyth, M.R., 1995. Biosens. Bioelectron. 10, 937–943. https://doi.org/10.1016/0956-5663(95)99231-9.

Medina-Sánchez, M., Martínez-Domingo, C., Ramon, E., Merkoçi, A., 2014. Adv. Funct. Mater. 24, 6291–6302. https://doi.org/10.1002/adfm.201401180.

Mishra, J., Mori, K., Ma, Q., Kelly, C., Barasch, J., Devarajan, P., 2004. Am. J. Nephrol. 24, 307–315. https://doi.org/10.1159/000078452.

Parolo, Claudio, Idili, A., Ortega, G., Csordas, A., Hsu, A., Arroyo-Currás, N., Yang, Q., Ferguson, B.S., Wang, J., Plaxco, K.W., 2020. ACS Sens. 5, 1877–1881. https://doi.org/10.1021/acssensors.0c01085.

Parolo, C., Sena-Torralba, A., Bergua, J.F., Calucho, E., Fuentes-Chust, C., Hu, L., Rivas, L., Álvarez-Diduk, R., Nguyen, E.P., Cinti, S., Quesada-González, D., Merkoçi, A., 2020. Nat. Protoc. https://doi.org/10.1038/s41596-020-0357-x.

Quesada-González, D., Merkoçi, A., 2017. Biosens. Bioelectron. 92, 549–562. https://doi.org/10.1016/j.bios.2016.10.062.

Rosati, G., Daprà, J., Cherré, S., Rozlosnik, N., 2014. Electroanalysis 26, 1400–1408. https://doi.org/10.1002/elan.201400062.

Rosati, G., Ravarotto, M., Sanavia, M., Scaramuzza, M., De Toni, A., Paccagnella, A., 2019a. Sens. Bio-Sensing Res. 26, 100308. https://doi.org/10.1016/j.sbsr.2019.100308.

Rosati, G., Ravarotto, M., Scaramuzza, M., De Toni, A., Paccagnella, A., 2019b. Sensor. Actuator. B Chem. 280, 280–289. https://doi.org/10.1016/j.snb.2018.09.084.

Sabaté del Río, J., Henry, O.Y.F., Jolly, P., Ingber, D.E., 2019. Nat. Nanotechnol. 14, 1143–1149. https://doi.org/10.1038/s41565-019-0566-z.

Sui, Y., Zorman, C.A., 2020. J. Electrochem. Soc. 167, 037571 https://doi.org/10.1149/1945-7111/ab721f.

Tortorich, R.P., Shamkhalichenar, H., Choi, J.W., 2018. Appl. Sci. 8 https://doi.org/10.3390/app8020288.

Vaidyanathan, R., Shiddiky, M.J.A., Rauf, S., Dray, E., Tay, Z., Trau, M., 2014. Anal. Chem. 86, 2042–2049. https://doi.org/10.1021/ac4032516.

Wang, J., Yu, J., Yang, Q., McDermott, J., Scott, A., Vukovich, M., Lagrois, R., Gong, Q., Greenleaf, W., Eisenstein, M., Ferguson, B.S., Soh, H.T., 2017. Angew. Chem. Int. Ed. 56, 744–747. https://doi.org/10.1002/anie.201608880.

Wünscher, S., Abbel, R., Perelaer, J., Schubert, U.S., 2014. J. Mater. Chem. C 2, 10232–10261. https://doi.org/10.1039/C4TC01820F.